Research Article

Vol. 24, No. 23 | 14 Nov 2016 | OPTICS EXPRESS 26363

Optics EXPRESS

Numerical study on the optical and carrier recombination processes in GeSn alloy for E-SWIR and MWIR optoelectronic applications

STEFANO DOMINICI,[1,2] HANQING WEN,[1] FRANCESCO BERTAZZI,[1,3] MICHELE GOANO[1,3] AND ENRICO BELLOTTI[2,*]

[1] *Dipartimento di Elettronica e Telecomunicazioni, Politecnico di Torino, Corso Duca degli Abruzzi 24, 10129 Torino, Italy*
[2] *Department of Electrical and Computer Engineering, Boston University, 8 Saint Mary's Street, Boston, Massachusetts 02215, USA*
[3] *IEIIT-CNR, Politecnico di Torino, corso Duca degli Abruzzi 24, 10129 Torino, Italy*
[*] *bellotti@bu.edu*

Abstract: The $Ge_{1-x}Sn_x$ alloy is a promising material for optoelectronic applications. It offers a tunable wavelength in the infrared (IR) spectrum and high compatibility with complementary metal-oxide-semiconductor (CMOS) technology. However, difficulties in growing device quality $Ge_{1-x}Sn_x$ films has left the potentiality of this material unexplored. Recent advances in technological processes have renewed the interest toward this material paving the way to potential applications. In this work, we perform a numerical investigation on absorption coefficient, radiative recombination rate, and Auger recombination properties of intrinsic and doped $Ge_{1-x}Sn_x$ for application in the extended-short wavelength infrared and medium wavelength infrared spectrum ranges. We apply a Green's function based model to the $Ge_{1-x}Sn_x$ full electronic band structure determined through an empirical pseudopotential method and determine the dominant recombination mechanism between radiative and Auger processes over a wide range of injection levels.

© 2016 Optical Society of America

OCIS codes: (160.0160) Materials; (160.4760) Optical properties; (160.6000) Semiconductor materials; (160.1890) Detector materials; (250.0250) Optoelectronics; (160.3130) Integrated optics materials; (130.3060) Infrared; (260.3800) Luminescence.

References and links

1. D. Stange, S. Wirths, N. Von Den Driesch, G. Mussler, T. Stoica, Z. Ikonic, J. M. Hartmann, S. Mantl, D. Grützmacher, and D. Buca, "Optical transitions in direct-bandgap $Ge_{1-x}Sn_x$ alloys," ACS Photon. **2**, 1539–1545 (2015).
2. M. Bauer, J. Taraci, J. Tolle, A. Chizmeshya, S. Zollner, D. J. Smith, J. Menendez, C. Hu, and J. Kouvetakis, "Ge–Sn semiconductors for band-gap and lattice engineering," Appl. Phys. Lett. **81**, 2992–2994 (2002).
3. M. R. Bauer, J. Tolle, C. Bungay, A. V. Chizmeshya, D. J. Smith, J. Menéndez, and J. Kouvetakis, "Tunable band structure in diamond–cubic tin–germanium alloys grown on silicon substrates," Solid State Commun. **127**, 355–359 (2003).
4. S. Wirths, R. Geiger, N. von den Driesch, G. Mussler, T. Stoica, S. Mantl, Z. Ikonic, M. Luysberg, S. Chiussi, J. Hartmann, H. Sigg, J. Faist, D. Buca, and D. Grützmacher, "Lasing in direct-bandgap GeSn alloy grown on Si," Nature Photon. **9**, 88–92 (2015).
5. C. Goodman, "Device applications of direct gap group IV semiconductors," Japan. J. Appl. Phys. **22**, 583 (1983).
6. W. Du, Y. Zhou, S. A. Ghetmiri, A. Mosleh, B. R. Conley, A. Nazzal, R. A. Soref, G. Sun, J. Tolle, J. Margetis, H. A. Naseem, and S. Q. Yu, "Room-temperature electroluminescence from Ge/$Ge_{1-x}Sn_x$/Ge diodes on Si substrates," Appl. Phys. Lett. **104**, 241110 (2014).
7. J. P. Gupta, N. Bhargava, S. Kim, T. Adam, and J. Kolodzey, "Infrared electroluminescence from GeSn heterojunction diodes grown by molecular beam epitaxy," Appl. Phys. Lett. **102**, 251117 (2013).
8. G. He and H. A. Atwater, "Interband transitions in Sn_xGe_{1-x} alloys," Phys. Rev. Lett. **79**, 1937 (1997).
9. A. A. Tonkikh, C. Eisenschmidt, V. G. Talalaev, N. D. Zakharov, J. Schilling, G. Schmidt, and P. Werner, "Pseudomorphic GeSn/Ge (001) quantum wells: Examining indirect band gap bowing," Appl. Phys. Lett. **103**, 032106 (2013).
10. A. Chizmeshya, C. Ritter, J. Tolle, C. Cook, J. Menendez, and J. Kouvetakis, "Fundamental studies of P $(GeH_3)_3$, As $(GeH_3)_3$, and Sb $(GeH_3)_3$: Practical n–dopants for new group IV semiconductors," Chem. Mater. **18**, 6266–6277 (2006).

#273484 http://dx.doi.org/10.1364/OE.24.026363
Journal © 2016 Received 10 Aug 2016; revised 28 Oct 2016; accepted 28 Oct 2016; published 7 Nov 2016

11. J. Xie, J. Tolle, V. D'Costa, C. Weng, A. Chizmeshya, J. Menendez, and J. Kouvetakis, "Molecular approaches to p-and n-nanoscale doping of $Ge_{1-y}Sn_y$ semiconductors: Structural, electrical and transport properties," Semiconductor Sci. Tech. **53**, 816–823 (2009).
12. H. Tran, W. Du, S. A. Ghetmiri, A. Mosleh, G. Sun, R. A. Soref, J. Margetis, J. Tolle, B. Li, H. A. Naseem, and S. Q. Yu, "Systematic study of $Ge_{1-x}Sn_x$ absorption coefficient and refractive index for the device applications of Si-based optoelectronics," J. Appl. Phys. **119**, 103106 (2016).
13. C. Senaratne, P. Wallace, J. Gallagher, P. Sims, J. Kouvetakis, and J. Menendez, "Direct gap $Ge_{1-y}Sn_y$ alloys: Fabrication and design of mid–IR photodiodes," J. Appl. Phys. **120**, 025701 (2016).
14. Y. Zhou, W. Dou, W. Du, T. Pham, S. A. Ghetmiri, S. Al-Kabi, A. Mosleh, M. Alher, J. Margetis, J. Tolle, G. Sun, R. Soref, B. Li, M. Mortazavi, H. Naseem, and S. Q. Yu, "Systematic study of GeSn heterostructure-based light-emitting diodes towards mid–infrared applications," J. Appl. Phys. **120**, 023102 (2016).
15. W. Du, Y. Zhou, S. A. Ghetmiri, A. Mosleh, B. R. Conley, A. Nazzal, R. A. Soref, G. Sun, J. Tolle, J. Margetis, H. A. Naseem, and S. Q. Yu, "Room–temperature electroluminescence from Ge/$Ge_{1-x}Sn_x$/Ge diodes on Si substrates," Appl. Phys. Lett. **104**, 241110 (2014).
16. S. Wirths, D. Buca, and S. Mantl, "Si–Ge–Sn alloys: From growth to applications," Progress in Crystal Growth and Characterization of Materials **62**, 1–39 (2016).
17. P. Moontragoon, Z. Ikonić, and P. Harrison, "Band structure calculations of Si–Ge–Sn alloys: achieving direct band gap materials," Semiconductor Sci. Tech. **22**, 742 (2007).
18. N. Bouarissa and F. Annane, "Electronic properties and elastic constants of the ordered $Ge_{1-x}Sn_x$ alloys," Mater. Sci. Eng. B **95**, 100–106 (2002).
19. J. D. Sau and M. L. Cohen, "Possibility of increased mobility in Ge–Sn alloy system," Phys. Rev. B **75**, 045208 (2007).
20. S. Gupta, B. Magyari-Köpe, Y. Nishi, and K. C. Saraswat, "Band structure and ballistic electron transport simulations in GeSn alloys," Proc. Simul. Semicond. Processes Devices pp. 3–6 (2012).
21. F. Freitas, J. Furthmüller, F. Bechstedt, M. Marques, and L. Teles, "Influence of the composition fluctuations and decomposition on the tunable direct gap and oscillator strength of $Ge_{1-x}Sn_x$ alloys," Appl. Phys. Lett. **108**, 092101 (2016).
22. V. R. D'Costa, C. S. Cook, A. Birdwell, C. L. Littler, M. Canonico, S. Zollner, J. Kouvetakis, and J. Menéndez, "Optical critical points of thin-film $Ge_{1-y}Sn_y$ alloys: A comparative $Ge_{1-y}Sn_y$/$Ge_{1-x}Sn_x$ study," Phys. Rev. B **73**, 125207 (2006).
23. T. Tsukamoto, N. Hirose, A. Kasamatsu, T. Mimura, T. Matsui, and Y. Suda, "Formation of GeSn layers on Si (001) substrates at high growth temperature and high deposition rate by sputter epitaxy method," J. Mater. Sci. **50**, 4366–4370 (2015).
24. J. Mathews, R. Beeler, J. Tolle, C. Xu, R. Roucka, J. Kouvetakis, and J. Menéndez, "Direct-gap photoluminescence with tunable emission wavelength in $Ge_{1-y}Sn_y$ alloys on silicon," Appl. Phys. Lett. **97**, 221912 (2010).
25. S. A. Ghetmiri, W. Du, J. Margetis, A. Mosleh, L. Cousar, B. R. Conley, L. Domulevicz, A. Nazzal, G. Sun, R. A. Soref, J. Tolle, B. Li, H. A. Naseem, and S. Q. Yu, "Direct-bandgap GeSn grown on silicon with 2230 nm photoluminescence," Appl. Phys. Lett. **105**, 151109 (2014).
26. H. Lin, R. Chen, W. Lu, Y. Huo, T. I. Kamins, and J. S. Harris, "Investigation of the direct band gaps in $Ge_{1-x}Sn_x$ alloys with strain control by photoreflectance spectroscopy," Appl. Phys. Lett. **100**, 102109 (2012).
27. M. L. Cohen, J. R. Chelikowsky, and J. R. Meyer-Arendt, "Electronic structure and optical properties of semiconductors," Applied Optics **28**, 2388 (1989).
28. H. Wen and E. Bellotti, "Rigorous theory of the radiative and gain characteristics of silicon and germanium lasing media," Phys. Rev. B **91**, 035307 (2015).
29. H. Wen, B. Pinkie, and E. Bellotti, "Direct and phonon-assisted indirect Auger and radiative recombination lifetime in HgCdTe, InAsSb, and InGaAs computed using Green's function formalism," J. Appl. Phys. **118**, 015702 (2015).
30. M. Otfried, *Semiconductors: data handbook* (Springer, 2004).
31. P. Landsberg and A. Beattie, "Auger effect in semiconductors," J. Phys. Chem. Solids **8**, 73–75 (1959).
32. M. Takeshima, "Unified theory of the impurity and phonon scattering effects on Auger recombination in semiconductors," Phys. Rev. B **25**, 5390 (1982).
33. M. Takeshima, "Green's-function formalism of band-to-band Auger recombination in semiconductors. correlation effect," Phys. Rev. B **26**, 917 (1982).
34. W. Bardyszewski and D. Yevick, "Compositional dependence of the Auger coefficient for InGaAsP lattice matched to InP," J. Appl. Phys. **58**, 2713–2723 (1985).
35. F. Bertazzi, M. Goano, and E. Bellotti, "A numerical study of Auger recombination in bulk InGaN," Appl. Phys. Lett. **97**, 231118 (2010).
36. F. Bertazzi, M. Goano, and E. Bellotti, "Numerical analysis of indirect Auger transitions in InGaN," Appl. Phys. Lett. **101**, 011111 (2012).
37. F. Bertazzi, X. Zhou, M. Goano, G. Ghione, and E. Bellotti, "Auger recombination in InGaN/GaN quantum wells. A full-Brillouin-zone study," Appl. Phys. Lett. **103**, 081106 (2013).
38. J. P. Walter and M. L. Cohen, "Frequency and wave-vector dependent dielectric function for silicon," Phys. Rev. B **5**, 3101 (1972).
39. C. Jungemann and B. Meinerzhagen, *Hierarchical device simulation: the Monte-Carlo perspective* (Springer Sci-

ence & Business Media, 2012).
40. H. Wen and E. Bellotti, “Optical absorption and intrinsic recombination in relaxed and strained InAs$_{1-x}$Sb$_x$ alloys for mid-wavelength infrared application,” Applied Physics Letters **107**, 222103 (2015).
41. M. V. Fischetti and S. E. Laux, “Band structure, deformation potentials, and carrier mobility in strained Si, Ge, and SiGe alloys,” J. Appl. Phys. **80**, 2234–2252 (1996).
42. L. Huldt, “Auger recombination in germanium,” Phys. Status Solidi A **24**, 221–229 (1974).
43. L. Huldt, “Phonon-assisted Auger recombination in germanium,” Phys. Status Solidi A **33**, 607–614 (1976).
44. A. Haug, “Phonon-assisted Auger recombination in degenerate semiconductors,” Solid State Commun. **22**, 537–539 (1977).
45. A. Haug, “Auger recombination of electron-hole drops,” Solid State Commun. **25**, 477–479 (1978).
46. C. Senaratne, P. Wallace, J. Gallagher, P. Sims, J. Kouvetakis, and J. Menendez, “Direct gap Ge$_{1-y}$Sn$_y$ alloys: Fabrication and design of mid-IR photodiodes,” J. Appl. Phys. **120**, 025701 (2016).
47. S. Dominici, H. Wen, F. Bertazzi, M. Goano, and E. Bellotti, “Numerical evaluation of Auger recombination coefficients in relaxed and strained germanium,” Appl. Phys. Lett. **108**, 211103 (2016).

---

1. Introduction

Germanium-based semiconductor compounds have been considered as potential candidates for optoelectronics applications on silicon platforms. In particular, alloys of germanium and tin - a IV group semi-metal - have always been regarded with great interest due the possibility of obtaining a tunable direct band gap. Experimental investigations have shown that the fundamental energy gap changes from indirect to direct as the Sn molar fraction increases. [1] In fact, the incorporation of Sn in Ge reduces the energy gap between the conduction band minima of Γ and L valleys up to the point where the crossover take place. A strong interest toward Ge$_{1\text{-x}}$Sn$_{\text{x}}$ is clearly due to its potential compatibility with complementary metal-oxide semiconductor (CMOS) technology and the possibility of monolithic integration on Si-based electronics. [2–4]

The early work of Goodman [5] provided the motivations to further studies on the electronic properties of GeSn. From an experimental perspective, the growth of GeSn layers characterized by high lattice crystallinity and low structural disorder has always been challenging. Due to the limited 1% equilibrium solubility of Sn in Ge, [6] and to the instability of α-Sn at high temperatures, which quickly degrades to β-Sn, experimentalists had to rely upon non-equilibrium growth techniques, such as molecular beam epitaxy. [7] Furthermore, problems of compositional homogeneity and phase purity prevented the formation of a stable alloy [8] above 20% of Sn composition. He and coworkers [8] performed one of the first growth and characterization of Ge$_{1\text{-x}}$Sn$_{\text{x}}$ films at different molar fractions. Of the characterized samples, they determined the optical absorption coefficient, then correlated the low energy tail in the absorption spectrum to the structural disorder of the samples through an Urbach tail model. The persistent presence of misfits dislocation defects in fabricated Ge$_{1\text{-x}}$Sn$_{\text{x}}$ samples have been confirmed in by Bauer and coworkers [2, 3] by TEM analysis, detecting also possible phenomena of phase separation between Ge and Sn. Novel deposition techniques allowed to grow pseudomorphic Ge$_{1\text{-x}}$Sn$_{\text{x}}$ on Ge(001) [9] and relaxed Ge$_{1\text{-x}}$Sn$_{\text{x}}$ on Si(001) [4]. Furthermore, *ad-hoc* techniques for the incorporation of *n*-type and *p*-type dopant species in Ge$_{1\text{-x}}$Sn$_{\text{x}}$ lattice have been developed. [7,10–12] The performances of Ge$_{1\text{-x}}$Sn$_{\text{x}}$ based p-i-n structures, grown on Si(100) substrate, for photodetection applications have been studied and presented in a number of articles. [13–15] Finally, S. Wirths, D. Buca, and S. Mantl [16] have compiled and extensive review on the history, fabrication techniques, and applications of Si-Ge-Sn based alloys.

The electronic properties of Ge$_{1\text{-x}}$Sn$_{\text{x}}$ have been investigated using a variety of theoretical models, including *ab-initio* techniques. [17–20] A great deal of effort has been directed toward the study of the energy dependence of the two conduction band minima, at L and Γ, as a function of the Sn molar fraction and the effect of an applied strain. However, it appears that the cluster expansion method adopted by Freitas and coworkers [21] found an agreement with the majority of experimental results. In their framework, the fundamental gaps at Γ and L are considered statistical quantities characterized by an average and a standard deviation as reported as shaded regions in Fig. 1. This statistical approach makes it possible to deal efficiently with the variety of experimental data, encompassing most of them within their range of uncertainty.

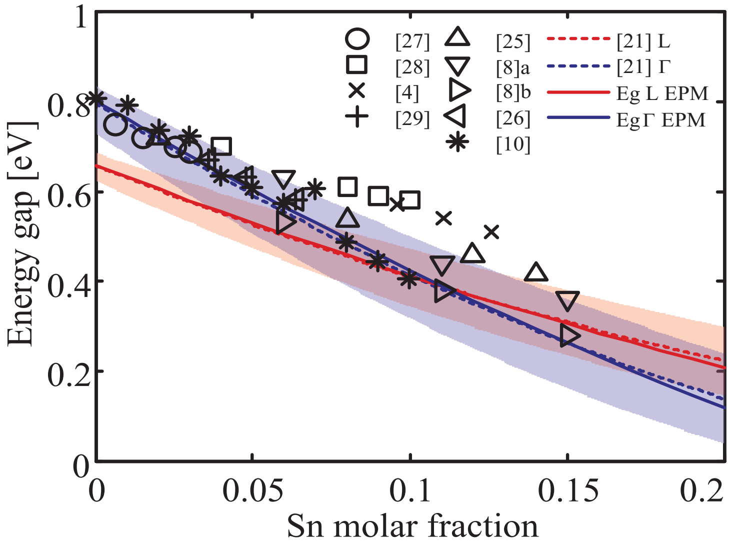

Fig. 1. Experimental and calculated energy gaps at Γ and L valleys as a function of the Sn molar fraction. Shaded area and dashed lines represent standard deviation and average value of results from Freitas and coworkers. [21] The solid lines represent the values computed in this work. A number of values presented in literature for the energy gap have been reported. [4, 8, 12, 22–26]

The goal of this works is to provide a comprehensive study of the optical properties and carrier recombination mechanisms in $Ge_{1\text{-}x}Sn_x$ alloy for applications in the extended-short (E-SWIR) and medium (MWIR) infrared wavelength. Specifically, we consider alloys characterized by an energy gap with a nominal cutoff wavelength of 2.7 μm and 5 μm at temperatures of 240 K and 140 K, respectively. This choice has been driven by the potential use of these materials for imaging applications where layers with these alloy compositions can be integrated on silicon read-out circuits. Using a numerical model we determine the absorption coefficient, the radiative recombination rate, and the Auger recombination rate of the material under different injection levels. We investigate the alloy properties in different doping conditions: intrinsic, *p*-doped and *n*-doped with concentrations of 10^{15} cm^{-3} and 10^{17} cm^{-3}, for both cases. While the numerical model can deal with strained material as well, for detector applications, where thick layer are needed, we speculate that the material will likely be relaxed. Therefore, we restrict the present effort to relaxed material and present the study of the strained material in a following work.

The manuscript is organized as follows: Section 2 will describe the numerical model used to determine the electronic properties, the absorption coefficient, and the recombination rates of Auger and radiative processes. Section 3 discusses the results and their implications, assessing the role played by radiative and non radiative processes at different injection levels. Finally, Section 4 will conclude.

2. Numerical model

We have determined the electronic structure of $Ge_{1\text{-}x}Sn_x$ alloys throughout the full composition range using a modified empirical pseudopotential method (EPM) [27] as implemented by Wen and Bellotti. [28, 29] The numerical model explicitly accounts for alloy disorder by means of

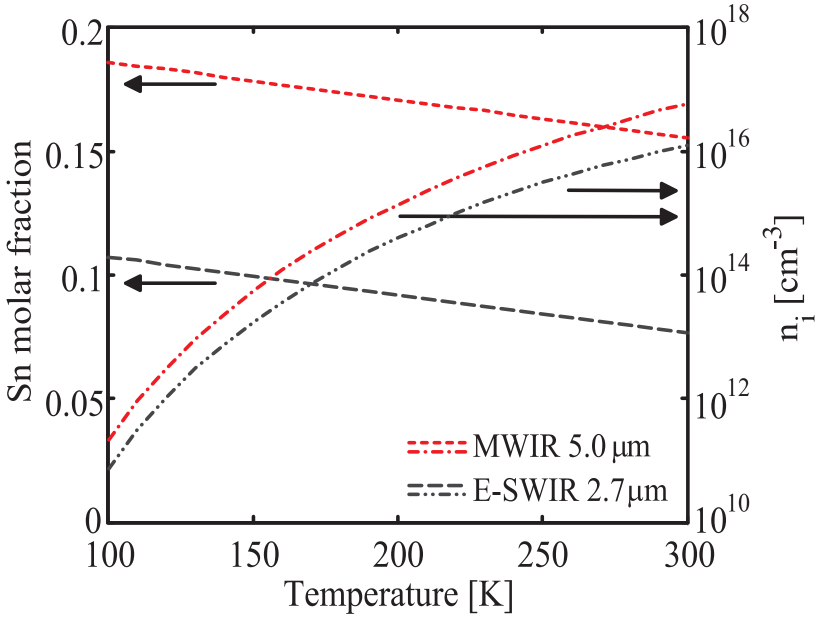

Fig. 2. Sn molar fraction required to obtain the proper cutoff wavelength, function of temperature, and the corresponding intrinsic carrier concentration.

two parameters: a disorder and spin parameters, respectively. These parameters have been used in the quadratic interpolation of atomic and spin-orbit screened atomic potentials as follows.

$$P_i^{(1,2)} = P_i^{(1,2)} - d_{(D,SO)}[x(1-x)]\left(P_i^{(1)} - P_i^{(2)}\right). \tag{1}$$

In Eq. (1), d_D is the disorder parameter, d_{SO} the spin parameter, x is the Sn molar fraction, and $P_i^{(1)}$ and $P_i^{(2)}$ are the screened atomic potentials for each atomic specie - either Sn or Ge. We set the disorder and spin disorder parameters in order to reproduce the trend of the fundamental energy gaps, measured at L and Γ valleys, to the average values given by Freitas and coworkers [21] as reported in Fig. 1. Therefore, the tin molar fractions that correspond to the cutoff wavelengths of 2.7 and 5 μm are 9% and 18% at the corresponding temperatures of 140 K and 240 K, respectively. We have included the effect of temperature on the energy gap through a rigid shift of all conduction states. We consider first the energy shift required to match the experimentally measured energy gap of pure Ge at 300 K [30] and linearly interpolated it to the temperatures of 140 K and 240 K. [12] Fig. 2 provides the value of the tin molar fraction, and corresponding intrinsic carrier concentration, as a function of the temperature needed to achieve a cut off wavelengths of 2.7 and 5 μm in the E-SWIR and MWIR spectral regions. Specifically, on the left vertical axis we have the molar fraction required to achieve the chosen band gap at a given temperature, and on the right vertical axis the corresponding intrinsic carrier concentration at a given temperature.

2.1. Auger recombination rate and lifetime

Theoretical models of Auger processes were first developed by Beattie and Landsberg. [31] Within the framework of second order perturbation theory (SOPT) they proposed an analytical expression for Auger lifetimes in semiconductors, normally referred to as the BLB model. However, their model assumes parabolic bands and applies to direct gap semiconductors. Successively, a Green's function based approach was introduces by Takeshima [32,33] and

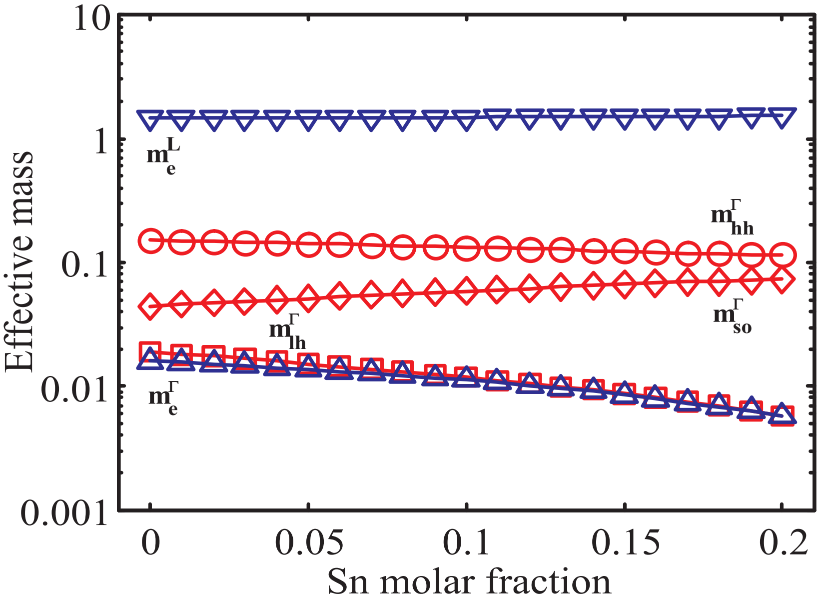

Fig. 3. Effective masses at critical points for Sn molar fractions comprised between 0% and 20%.

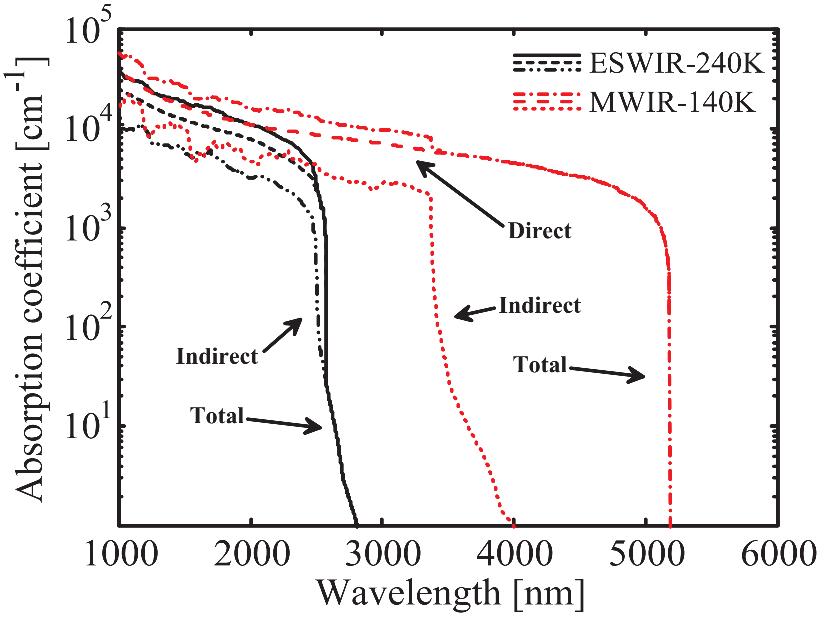

Fig. 4. Absorption coefficient for intrinsic $Ge_{1-x}Sn_x$ in E-SWIR and MWIR configurations.

Bardyszewsky and Yevick [34]. This approach overcomes the numerical singularity of SOPT and allow to embed the contribution of carrier-phonon interactions into the spectral density function. In this work, we have employed a Green's function based model to determine the Auger recombination rate and lifetime for the bulk material. We considered two categories of Auger processes: direct and indirect. In the first category, the transition is mediated just by Coulomb interactions while in the second an additional interaction, such as phonon or impurity scattering, takes part in the process. Furthermore, we have calculated separate contributions for electron and hole based processes, respectively labeled as *eeh* and *hhe*. The numerical model we have employed in based on the formalism proposed by Takeshima, [32, 33] successively extended to the case of full band structure by Wen and coworkers. [28, 29, 35–37] The total Auger recombination rate per unit volume and time in bulk material is given by:

$$\begin{aligned} R_{AR} = {} & \frac{2\pi}{\hbar}\frac{V^3}{(2\pi)^9}\left[1 - e^{(\mu_v-\mu_c)/k_BT}\right]\int \mathrm{d}\mathbf{k}_1\mathrm{d}\mathbf{k}_2\mathrm{d}\mathbf{k}_{1'}\mathrm{d}\mathbf{k}_{2'}\, |M_{ee}|^2\, \delta(\mathbf{k}_1 + \mathbf{k}_2 - \mathbf{k}_{1'} - \mathbf{k}_{2'}) \\ & \times \int \mathrm{d}E_1\mathrm{d}E_2\mathrm{d}E_{1'}\mathrm{d}E_{2'}\Theta(E_1)\Theta(E_2)[1-\Theta(E_{1'})][1-\Theta(E_{2'})] \\ & \times \mathrm{Im}G^R_{l_1}(\mathbf{k}_1, E_1)\mathrm{Im}G^R_{l_2}(\mathbf{k}_2, E_2)\mathrm{Im}G^R_{l_{1'}}(\mathbf{k}_{1'}, E_{1'})\mathrm{Im}G^R_{l_{2'}}(\mathbf{k}_{2'}, E_{2'}). \end{aligned} \tag{2}$$

where $\mathrm{Im}G^R_{l_{1'}}(\mathbf{k}_{1'}, E_{1'})$ is the spectral density function representing the energy broadening of state $l_{1'}$ at $\mathbf{k}_{1'}$, $\Theta(E)$ represent the Fermi-Dirac occupation statistical factor, $|M_{ee}|^2$ is the matrix element for the Auger process representing the square overlap integral between the four state wavefunctions involved in the transition. The Coulomb interaction between carriers with different wave-vectors is screened by a wave-vector dependent, static dielectric function, implemented using a analytical expression given by:

$$\varepsilon(\mathbf{q}) = 1 + \frac{c_1}{|\mathbf{q}|^{c_2} + c_3}, \tag{3}$$

in which c_1, c_2 and c_3 are parameters obtained by fitting results from random phase approximation [38]. The presence of the twelve-fold k-space integrals in Eq. (2) makes it very difficult to use a direct integration approach. The numerical evaluation of Eq. (2) is performed using an hybrid approach that employs a Monte Carlo procedure and a direct integration based on the tetrahedron method [39]. The indirect processes are evaluated including the contribution of carrier-phonon interaction through four self-energy functions, introducing an energy broadening for the states involved in the transition (Sec.2.3). From the knowledge of the total recombination rate it is possible to compute the Auger coefficients C_n and C_p starting from the expression:

$$R_{AR} = \left(nC_n + pC_p\right)\left(np - n_i^2\right), \tag{4}$$

In the same way, the carrier lifetimes can be obtained for an arbitrary doping and injection condition from the expression:

$$\tau_{\mathrm{eeh}} = \frac{np - n_i^2}{nR_{AR}^{(\mathrm{eeh})}}, \qquad \tau_{\mathrm{hhe}} = \frac{np - n_i^2}{pR_{AR}^{(\mathrm{hhe})}}. \tag{5}$$

2.2. Absorption coefficient and radiative recombination rate and lifetime

Unlike Auger, radiative recombination processes are mediated by dipole interactions, where a photon is absorbed or emitted to conserve the total energy of the transition. A Green's function based model has already been presented in [28] and applied by Wen and coworkers to determine the optical properties of $\mathrm{InAs}_{1-x}\mathrm{Sb}_x$ alloy, silicon and germanium [28, 40]. The radiative recombination rate is given by:

$$
\begin{aligned}
R_{RR} = {} & \frac{2e^2 n_r \omega_{ph}}{\pi\hbar m_0^2 c_0^3 V \varepsilon_0} \sum_{\mathbf{k}_v,\mathbf{k}_c} |\langle \mathbf{k}_v | \hat{\mathbf{e}} \cdot \mathbf{P} | \mathbf{k}_c \rangle|^2 \int \mathrm{d}E_1 \int \mathrm{d}E_2 \Theta(E_2)[1-\Theta(E_1)] \\
& \times \delta\Big(\mathbf{k}_c - \mathbf{k}_v - \mathbf{k}_{\mathrm{ph}}\Big) \delta\Big(\mu_c - \mu_v + E_2 - E_1 - \hbar\omega_{\mathrm{ph}}\Big) \mathrm{Im} G^R_{l_v}(\mathbf{k}_v, E_1) \mathrm{Im} G^R_{l_c}(\mathbf{k}_c, E_2). \qquad (6)
\end{aligned}
$$

The the absorption coefficient can be directly evaluated using Eq. (6) with a different pre-factor and accounting for the proper initial and final valence and conduction states. The carrier-phonon interaction is included through two self-energy functions, one for conduction and one for valence states. The classical result for the direct process, obtained from Fermi golden rule can be retrieved by substituting the self-energies with delta functions. Our results include broadening for both initial and final states. We calculate the radiative coefficient and lifetimes, assuming the same concentration of electrons and holes, as follows:

$$
\tau_n = \frac{np - n_i^2}{nR_{RR}}, \qquad \tau_p = \frac{np - n_i^2}{pR_{RR}}. \qquad (7)
$$

2.3. Spectral density function

The core of the Green's function based approach consists in the evaluation of the spectral density function, related to the imaginary part of the retarded Green's functions ($\mathrm{Im}G^R_{l_i}$), that depends on the system self-energy (Σ_i).

$$
\mathrm{Im}G^R_{l_i}(\mathbf{k}, E) = -\frac{1}{\pi} \frac{\mathrm{Im}\Sigma_i(\mathbf{k}, E)}{[E - E_i - \mathrm{Re}\Sigma_i(\mathbf{k}, E)]^2 + [\mathrm{Im}\Sigma_i(\mathbf{k}, E)]^2}. \qquad (8)
$$

The imaginary part of the retarded Green's function, presented in Eq. (8), has a lorentzian distribution shape, centered at E_i. The real and imaginary part of the self-energy term describe respectively the shift and the broadening of the distribution over the energy domain, modeling the effects of all perturbations (e.g. carrier-phonon scattering) acting on the system. The conventional approach to evaluate the self-energy is by means of the Dyson's equation, truncating the expansion up to the desired order [28,32]. In the case of our interest, namely the calculation of Auger and ratiative recombination rates and absorption coefficient, we have truncated the expansion to the lowest order [29]. The interactions taken into account to evaluate the self-energy are non-polar optical and acoustic phonon scattering mechanisms. Their numerical contribution to the self-energy is obtained by using the appropriate matrix element, given by [28]:

$$
|g_{\mathrm{AC}}(q)|^2 = \frac{\Xi_d^2 \hbar\omega_{ac}(q)}{2c_l} \frac{q^4}{(q^2 + \lambda^2)^2}, \qquad (9)
$$

$$
|g_{\mathrm{NPO}}(q)|^2 = \frac{\hbar D^2 v_s^2}{2\bar{c}\omega_{op}(q)} \frac{q^4}{(q^2 + \lambda^2)^2}, \qquad (10)
$$

In Eqs. (9)-(10), c_l and c_t are the longitudinal and transverse elastic constants, $\bar{c} = c_l/3 + 2c_t/3$ is the average lattice constant, v_s is the sound velocity. Table 1 reports the parameters used to evaluate the matrix elements for each mechanism presented in Eqs. (9)-(10).

Earlier calculations [42–45] made use of a simplified analytical model for the band structure (i.e. effective mass approximation). Their motivation was to avoid costly numerical calculations and investigate the limit cases. The use of analytical bands within the effective mass model is a drastic approximation, both for Ge and GeSn. In fact, in these materials both the Γ and L valleys significantly contribute the conduction band density of states, and consequently the number of available final states for the Auger transition, making both the direct and indirect processes important. Furthermore, the valence band structure and the relevant matrix elements play a significant role in determining the strength of direct and indirect transitions.

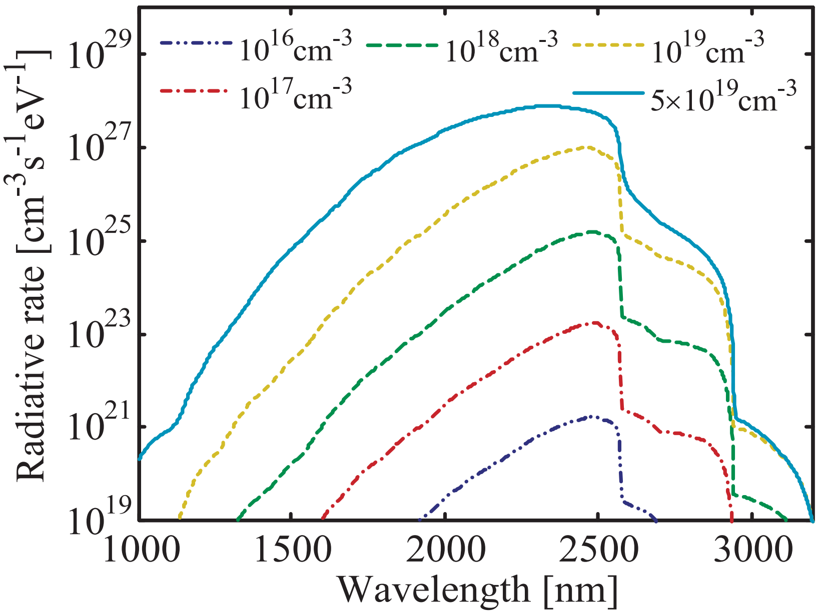

Fig. 5. Radiative recombination rate for intrinsic $Ge_{1-x}Sn_x$ in the E-SWIR configuration at 240K under different injection conditions.

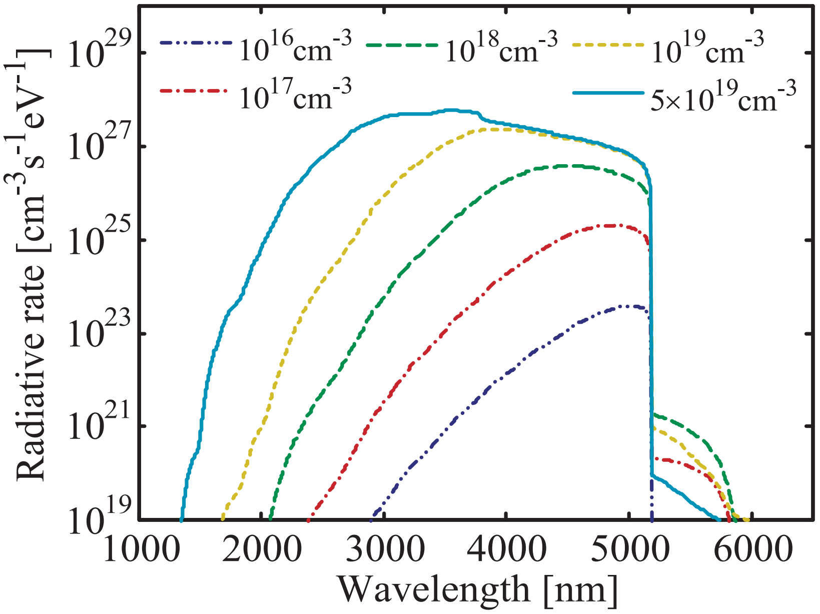

Fig. 6. Radiative recombination rate for intrinsic $Ge_{1-x}Sn_x$ in the MWIR configuration at 140K under different injection conditions.

3. Numerical results

Figure 1 presents a comparison between the calculated and experimental [4, 8, 12, 22–26] values of the energy gap values for $Ge_{1-x}Sn_x$ and the results of our EPM model. Based on our results,

Table 1. Alloy parameters for E-SWIR (9%) and MWIR (18%) $Ge_{1\text{-}x}Sn_x$. [30, 41] The values for the alloy has been obtained using a linear interpolation in the molar fraction.

Parameter	Unit	$Ge_{0.91}Sn_{0.09}$	$Ge_{0.82}Sn_{0.18}$
c_l	GPa	117.950	114.100
c_t	GPa	64.769	65.522
ε_0	-	16.880	17.440
ε_∞	-	16.880	17.440
$\hbar\omega_{\text{op}}$	meV	35.930	35.060
Ξ_d	eV	9.1	9.1
$D(L_{6c})$	10^8 eV/cm	12.17	12.17
$D(L_v)$	10^8 eV/cm	10	10

we can see that $Ge_{1\text{-}x}Sn_x$ is an indirect energy gap material at the E-SWIR cut off and a direct energy gap material in the MWIR case.

We have calculated the electronic structure of $Ge_{1\text{-}x}Sn_x$ for a Sn composition between 0% and 20% and evaluated the effective mass variations as a function of the molar fractions at Γ and L valley minimum. Subsequently, we have also averaged the effective masse values along different principal directions, that for the zincblende reciprocal lattice are denoted as: Σ, Δ, and Λ. For the *i*-th band the mass is computed determining the second derivative, as in Eq. (11), of the band profile using a second order interpolation close to the minima.

$$\frac{1}{m_i} = \frac{1}{m_i^{(\Sigma)}} + \frac{1}{m_i^{(\Delta)}} + \frac{1}{m_i^{(\Lambda)}} \tag{11}$$

$$m_i = m_i^0 + x\, m_i^1 \tag{12}$$

Once the effective masses are known for a discrete number of molar fractions a linear interpolation, as in Eq. (12), can be used to obtain values for arbitrary compositions. First and zeroth order fitting parameters for heavy hole (HH) band, light hole (LH) band, spin-orbit (SO) band, and first conduction band are reported in Tab. 3-2. The direction averaged effective mass function of Sn molar fraction for HH band, LH band, SO band, and first conduction band are presented in Fig. 3. The effective mass for HH band, LH band, and first conduction band at Γ decrease for increasing values of molar fraction, while the effective mass for SO band and first conduction band at L increase for increasing values of molar fraction.

Table 2. Zeroth order interpolation coefficients for direction dependent effective masses. Curves were fitted to Sn molar fraction comprised between 0% and 20%.

$\mathrm{m}^{\text{valley}}_{\text{direction}}$	HH	LH	SO	CB
$\mathrm{m}^{(0),\Gamma}_{(111)}$	0.7361	0.0533	0.1318	0.0487
$\mathrm{m}^{(0),\Gamma}_{(100)}$	0.2845	0.0600	0.1323	0.0486
$\mathrm{m}^{(0),\Gamma}_{(110)}$	0.5451	0.0545	0.1322	0.0486
$\mathrm{m}^{(0),L}_{(111)}$	-	-	-	1.4469

Table 3. First order interpolation coefficients for direction dependent effective masses. Curves were fitted to Sn molar fraction comprised between 0% and 20%.

$m^{\text{valley}}_{\text{direction}}$	HH	LH	SO	CB
$m^{(1),\Gamma}_{(111)}$	-0.1294	-0.1855	0.4387	-0.1532
$m^{(1),\Gamma}_{(100)}$	-0.4434	-0.2149	0.4364	-0.1533
$m^{(1),\Gamma}_{(110)}$	-0.5269	-0.1922	0.4369	-0.1546
$m^{(1),L}_{(111)}$	-	-	-	0.3572

3.1. *Optical emission and absorption properties*

We have also computed the optical emission and absorption properties, commonly referred to as the radiative recombination rate and absorption coefficient, of intrinsic $Ge_{1-x}Sn_x$ with cutoff in the E-SWIR ($Ge_{0.91}Sn_{0.09}$) and MWIR ($Ge_{0.82}Sn_{0.18}$) spectral range at a temperature of 240K and 140K, respectively. Figure 4 presents the calculated absorption coefficient for $Ge_{0.91}Sn_{0.09}$ and $Ge_{0.82}Sn_{0.18}$.The total absorption coefficient is represented by solid lines, while direct and indirect contributions are represented by dotted and dashed lines, respectively. The trend of direct and indirect components of the absorption coefficients in Fig. 4 confirms an indirect energy gap for the E-SWIR material in the E-SWIR, and a direct energy gap for the MWIR.

We have also calculated the radiative recombination rates for $Ge_{0.91}Sn_{0.09}$ and $Ge_{0.82}Sn_{0.18}$ through a direct numerical evaluation of Eq. (6) and reported the results in Fig. 5 and Fig. 6, respectively. Furthermore, we have considered the material under different injection levels: from 10^{16} cm^{-3} up to 5×10^{19}. In case of $Ge_{0.91}Sn_{0.09}$ (Fig. 5) to an increase in the injection level we observed an increase in the overall rate together with a minor blue shift of the wavelength at which the emission peak occurs. Instead, in case of $Ge_{0.82}Sn_{0.18}$ (Fig. 6) to an increase in the injection level we observed a strong blue shift of the peak wavelength and correlated it to the contribution coming from the indirect L valley, whose minimum is located at an energy higher than Γ valley minimum. The non-zero contributions below the energy gap, as seen in Fig. 5, correspond to recombination processes close to the band minima assisted by phonon emission/absorption.

3.2. *Auger and radiative recombination*

The total Auger recombination rate is calculated separately for electron and holes, the *eeh* and *hhe* Auger processes, as a sum of direct and indirect contributions. For each carrier type, we have considered two different processes, classified by the energy band of the secondary particle final state: first and second conduction bands for *eeh* processes and first and second valence bands for *hhe* processes. Furthermore, when dealing with a doped semiconductor, we have calculated the Auger recombination rate for the dominant mechanism, determined by the type of minority carriers: *eeh* for *p*-doped and *hhe* for *n*-doped. The Auger lifetimes are obtained using Eq. (5) once the rate is known from the numerical integration of Eq. (2). To perform a quantitative comparison, we also determine the radiative lifetime that is obtained directly from Eq. (7) using the radiative recombination rate computed using Eq. (6).

For the Auger rate, the convergence of the Monte Carlo integration is achieved once the ratio between the standard deviation and the average value of the result is below 0.1%. Moreover, we have considered doping concentrations of 10^{15} cm^{-3} and 10^{17} cm^{-3}, for both *n*-type and p-type, and the excess carrier concentration to values ranging from 10^{14} cm^{-3} to 10^{17} cm^{-3} for the lower doping and from 10^{16} cm^{-3} to 5×10^{19} cm^{-3} for the higher one. Figures 7 to 10, present the calculated radiative and Auger lifetimes for doped $Ge_{0.91}Sn_{0.09}$ and $Ge_{0.82}Sn_{0.18}$

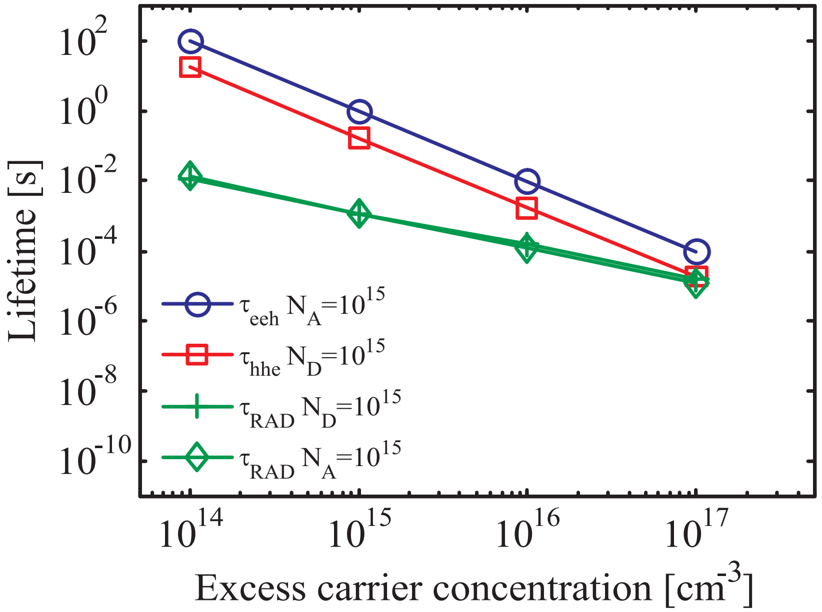

Fig. 7. Auger and radiative lifetimes function of excess carrier concentrations for doped $Ge_{0.91}Sn_{0.09}$ (E-SWIR configuration). The doping level is 10^{15} cm^{-3} for both *n*-type and *p*-type.

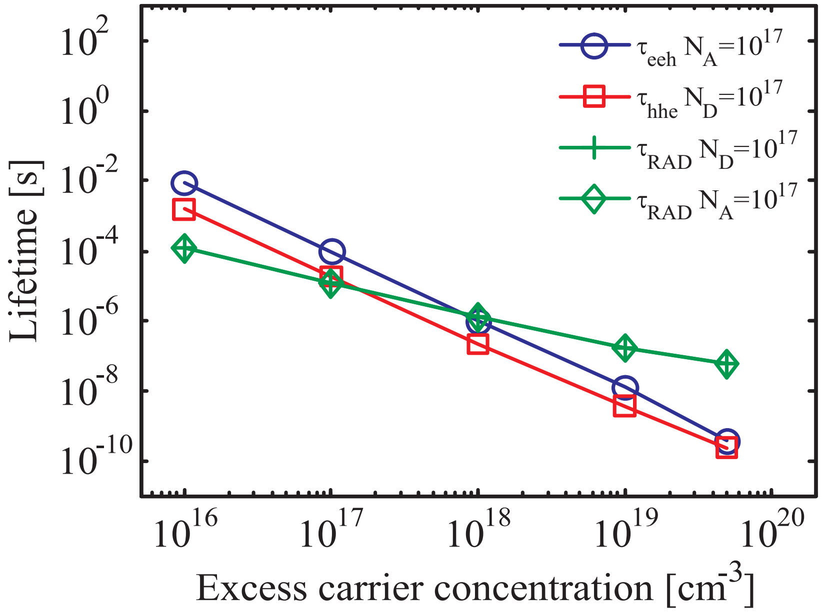

Fig. 8. Auger (*eeh* and *hhe*) and radiative lifetimes over a wide range of excess carrier concentrations in case of doped $Ge_{0.91}Sn_{0.09}$ (E-SWIR configuration). The doping level is 10^{17} cm^{-3} for both *n*-type and *p*-type.

compositions.

We have checked that all the important contributions have been taken into account for both

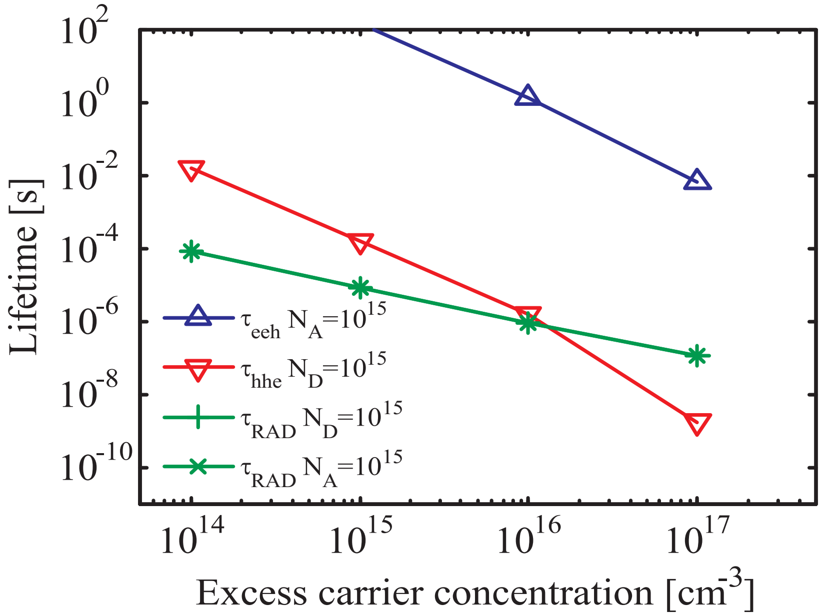

Fig. 9. Auger (*eeh* and *hhe*) and radiative lifetimes over a wide range of excess carrier concentrations in case of doped $Ge_{0.82}Sn_{0.18}$ (MWIR configuration). The doping level is 10^{15} cm^{-3} for both *n*-type and *p*-type.

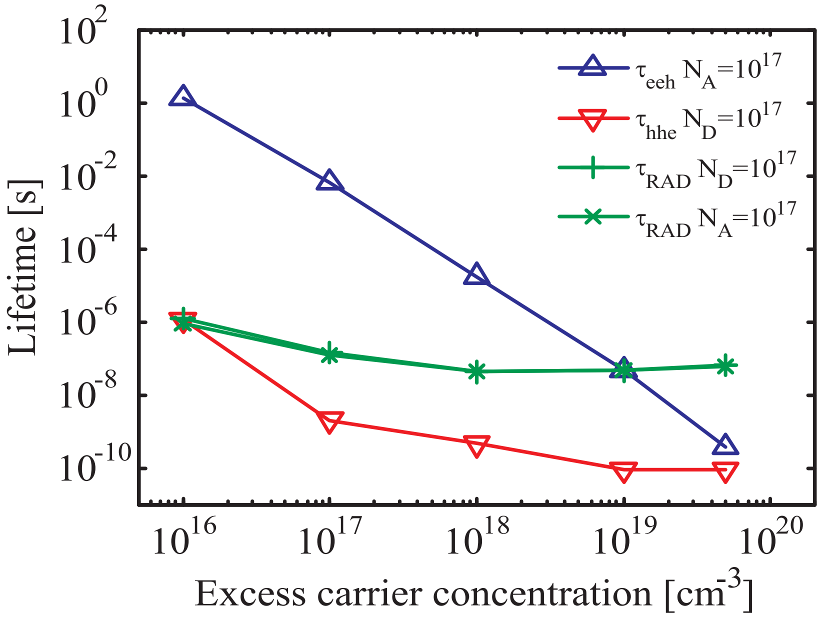

Fig. 10. Auger (*eeh* and *hhe*) and radiative lifetimes over a wide range of excess carrier concentrations in case of doped $Ge_{0.82}Sn_{0.18}$ (MWIR configuration). The doping level is 10^{17} cm^{-3} for both *n*-type and *p*-type.

eeh and *hhe* Auger transitions. In case of *eeh* processes, the large majority of energy states in the third conduction have energies higher than the gap. Therefore, only a limited set of final states is

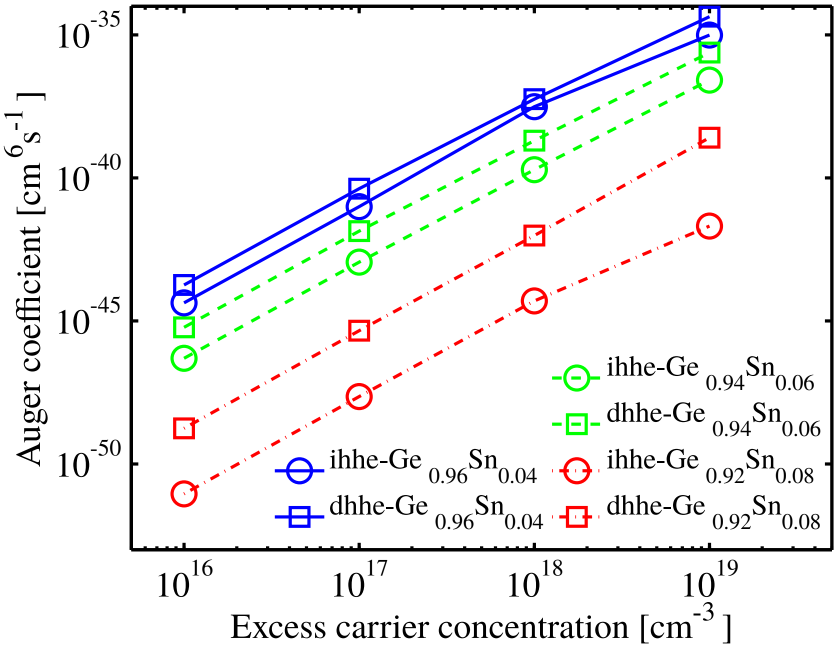

Fig. 11. Auger recombination coefficient as a function of excess carrier concentration for intrinsic $Ge_{1\text{-}x}Sn_x$ at 300 K and three molar fractions: $x = 0.04$, $x = 0.06$, and $x = 0.08$. The Auger coefficients decrease with increasing Sn molar fractions and the contribution from CHSH processes in case of $Ge_{0.91}Sn_{0.09}$ and $Ge_{0.82}Sn_{0.18}$ is negligible.

available in this band, resulting in a negligible contribution to the total Auger rate. On the other hand, it is worthwhile to investigate the contribution of CHSH transitions, or *hhe* processes, in which the final state is found in the split-off band. [22] Since the spin-orbit splitting energy in $Ge_{1\text{-}x}Sn_x$ increases with molar fraction, [22] the transition rate of *hhe* processes having the split-off band as final state is expected to decrease as well. [46]

We calculated the contribution to the Auger coefficients of direct and indirect *hhe* transitions for processes where the final state for the scattered hole is located in the split-off band . We have done so in the case of intrinsic $Ge_{1\text{-}x}Sn_x$ for $x = 0.04$, $x = 0.06$, and $x = 0.08$, at 300 K, and under four excess carrier concentrations, namely $n = p = 10^{16}$ cm^{-3}, $n = p = 10^{17}$ cm^{-3}, $n = p = 10^{18}$ cm^{-3}, and $n = p = 10^{19}$ cm^{-3}. From the results reported in Fig.11, we are able to conclude that the contribution of CHSH transitions diminishes with Sn molar fraction, regardless of the relative magnitude of the split-off energy and gap.

Considering the case of $Ge_{0.91}Sn_{0.09}$ with a doping concentration of 10^{15} cm^{-3}, as shown in Fig. 7, we observe that the radiative lifetime is smaller than Auger lifetimes at excess carrier concentrations below 10^{17} cm^{-3}. Therefore the radiative recombination process is the dominant mechanism in low injection regime. In the case of $Ge_{0.91}Sn_{0.09}$ doped at the 10^{17} cm^{-3} level, as we observe in Fig. 8, the radiative processes dominates over the Auger processes at excess carrier concentrations lower than 10^{17} cm^{-3} and that the two Auger processes - *eeh* and *hhe* - are rather similar in magnitude at any given excess carrier concentration. Considering instead the case of a $Ge_{0.82}Sn_{0.18}$ with a doping concentration of 10^{15} cm^{-3}, we observe in Fig. 9 that the radiative lifetime is smaller than Auger lifetimes at excess carrier concentrations below 10^{16} cm^{-3}. However, the *hhe* Auger recombination processes still play a significant role in the low injection regime due to the small difference between radiative and *hhe* Auger lifetimes. In case of $Ge_{0.82}Sn_{0.18}$ with a 10^{17} cm^{-3} doping level, as it can be seen in Fig. 10, the

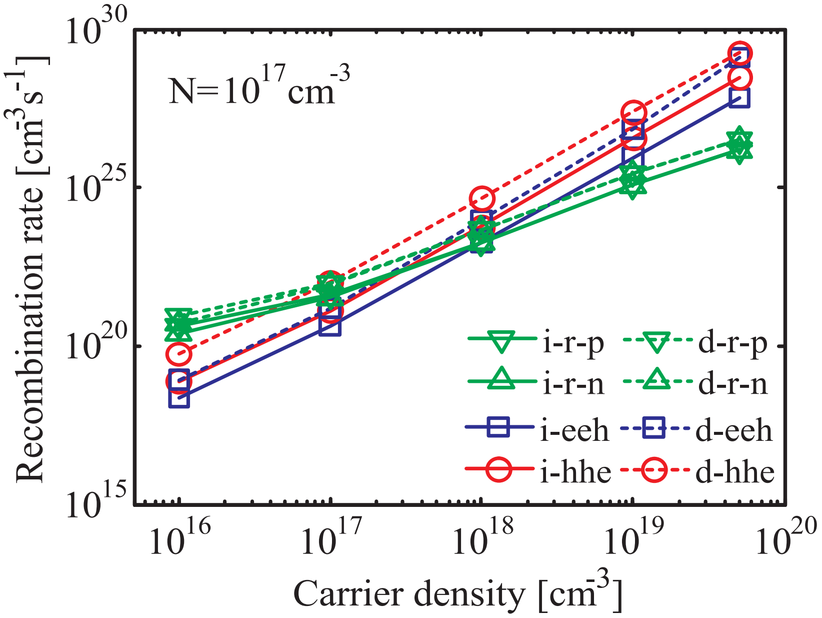

Fig. 12. Auger and radiative recombination rate function of excess carrier concentrations for doped $Ge_{0.91}Sn_{0.09}$ (E-SWIR configuration). The doping level is 10^{17} cm^{-3} for both *n*-type and *p*-type. The first label in each legend entry refers to indirect (i) and direct (d) processes, respectively. The second label refers to radiative (r) or Auger class (eeh or hhe). The last label, reported for radiative processes only, refers to the type of doping (*n* or *p* respectively).

radiative process becomes less important than the Auger processes for all the excess carrier concentrations considered and that the *hhe* Auger process is the overall dominant recombination mechanism. Furthermore, it is possible to observe a saturation behavior for the dominant Auger processes for increasing excess carrier concentrations and a change of monotonicity in the radiative lifetime for excess carrier concentrations above 10^{18} cm^{-3}. As a result, for excess carrier concentrations above 10^{18} cm^{-3} the radiative recombination rate decrease and the corresponding lifetime slightly increases. We report results on the radiative recombination rate, function of excess carrier concentration, and separate contribution from indirect (phonon-assisted) and direct processes in Fig. 12 and 13.

We speculate that the driving factor behind the differences between the lifetime trends of $Ge_{0.91}Sn_{0.09}$ and $Ge_{0.82}Sn_{0.18}$ compositions can be traced back to the difference in the energy gaps and the position of Γ with respect to the L minima. In fact, considering the small difference in the effective masses between the two compositions (as reported in Fig. 3) the curvature of the band structure around the Γ and L minimum undergoes a small variations going from a composition to the other. On the other hand, the reduction of the energy gap and the different positions of Γ and L valley minimum strongly affects the quasi-Fermi energies and the carrier distribution in the k-space. We have also computed the radiative and Auger coefficients, to be

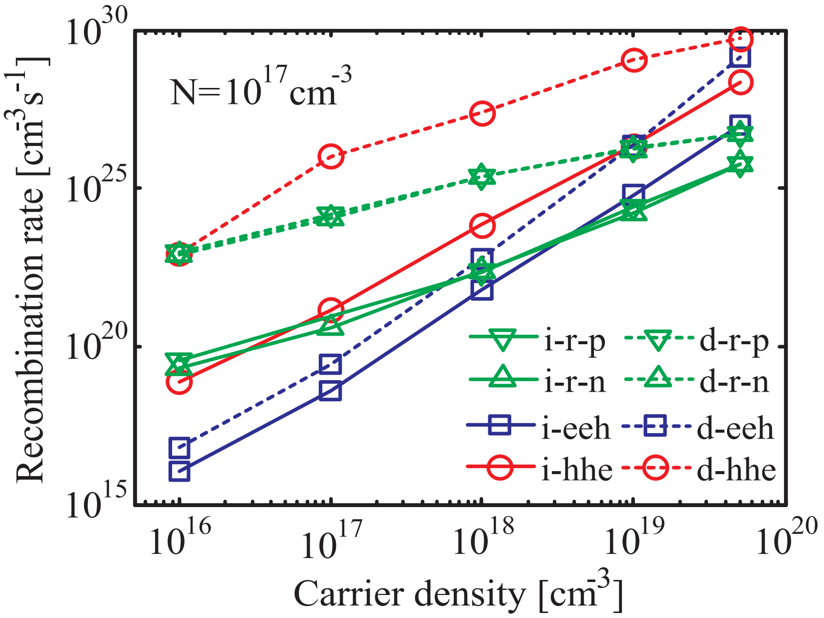

Fig. 13. Auger and radiative recombination rate function of excess carrier concentrations for doped $Ge_{0.82}Sn_{0.18}$ (MWIR configuration). The doping level is 10^{17} cm^{-3} for both *n*-type and *p*-type. The first label in each legend entry refers to indirect (i) and direct (d) processes, respectively. The second label refers to radiative (r) or Auger class (eeh or hhe). The last label, reported for radiative processes only, refers to the type of doping (*n* or *p* respectively).

used in device simulation models, accordingly to the following expressions:

$$B = \frac{R_{RR}}{np - n_i^2}, \tag{13}$$

$$C_{\text{eeh}} = \frac{R_{AR}^{(\text{eeh})}}{n\left(np - n_i^2\right)}, \tag{14}$$

$$C_{\text{hhe}} = \frac{R_{AR}^{(\text{hhe})}}{p\left(np - n_i^2\right)}. \tag{15}$$

Equations (13)-(15) ascribe the dependence of radiative and Auger recombination rates to second and third order polynomials on free carrier concentration, respectively. These equations are used to fit data on total recombianation rate, without distinction between direct and indirec processes. Given the total recombination rate from the numerical evaluation of Eq.(2) and Eq.(6), we calculate the Auger and radiative recombination coefficients directly from Eqs.(13)-(15). Therefore, coefficients calculated through Eqs.(13)-(15) are valid as long as the recombination rate computed from Eq. (2) and Eq. (6) are physically accurate. Figures 14 to 17 present the calculated values, as a function of injection level, for doped $Ge_{1\text{-}x}Sn_x$ in E-SWIR and MWIR configuration. The same Auger recombination model and calculation methodology have been used to evaluate Auger coefficients in relaxed and strained Ge [47]. As it can be observed in Fig. 14 and Fig. 16, in the low injection regime and doping concentration of 10^{15} cm^{-3} both radiative and Auger coefficient are almost constant with injection level. However, radiative and Auger recombination coefficients in $Ge_{0.82}Sn_{0.18}$ exhibit significant variations for injection lev-

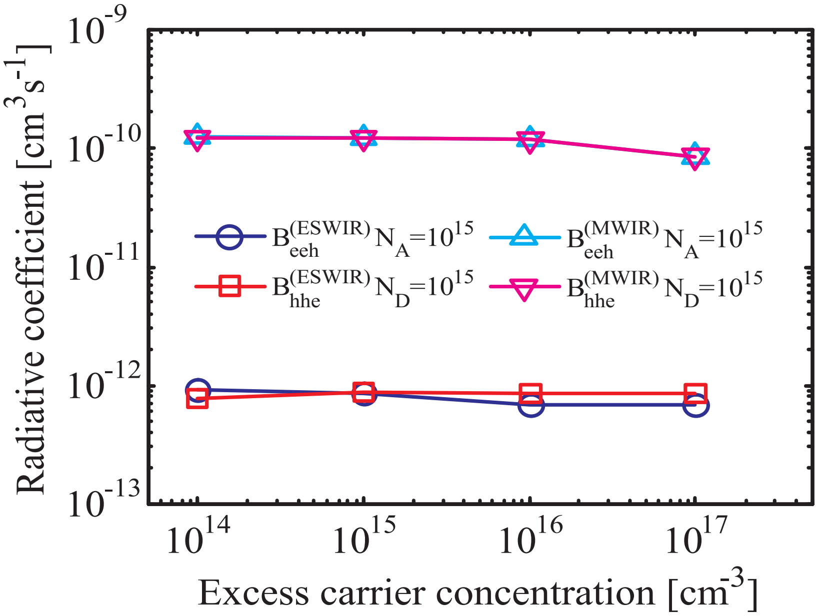

Fig. 14. Radiative recombination coefficient function of injection level for doped $Ge_{1-x}Sn_x$ in E-SWIR and MWIR configurations. The doping level is 10^{15} cm^{-3} for both *n*-type and *p*-type.

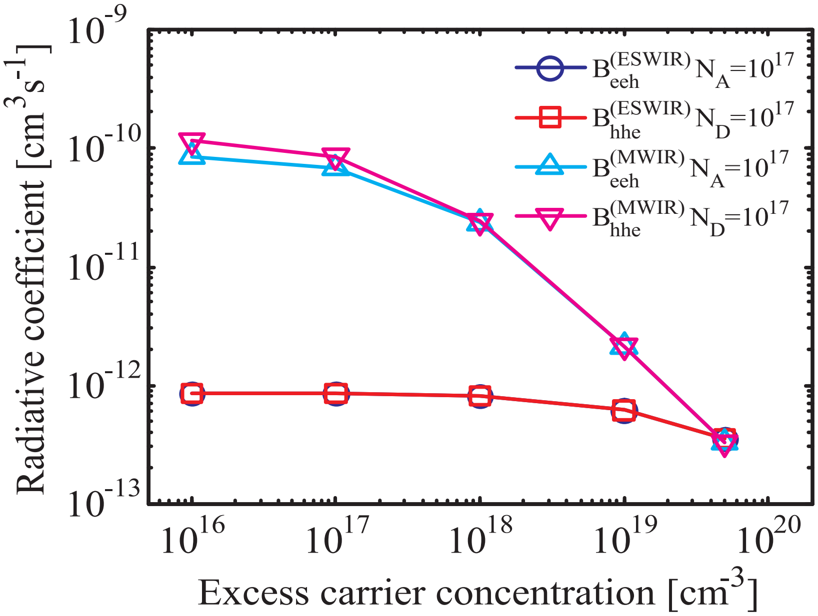

Fig. 15. Radiative recombination coefficient function of injection level for doped $Ge_{1-x}Sn_x$ in E-SWIR and MWIR configurations. The doping level is 10^{17} cm^{-3} for both *n*-type and *p*-type.

els higher than 10^{16} cm^{-3}. The complexity of Eq. (2), in which many different contributions are present, prevents us from being able to give a simple explanation of the differences between the

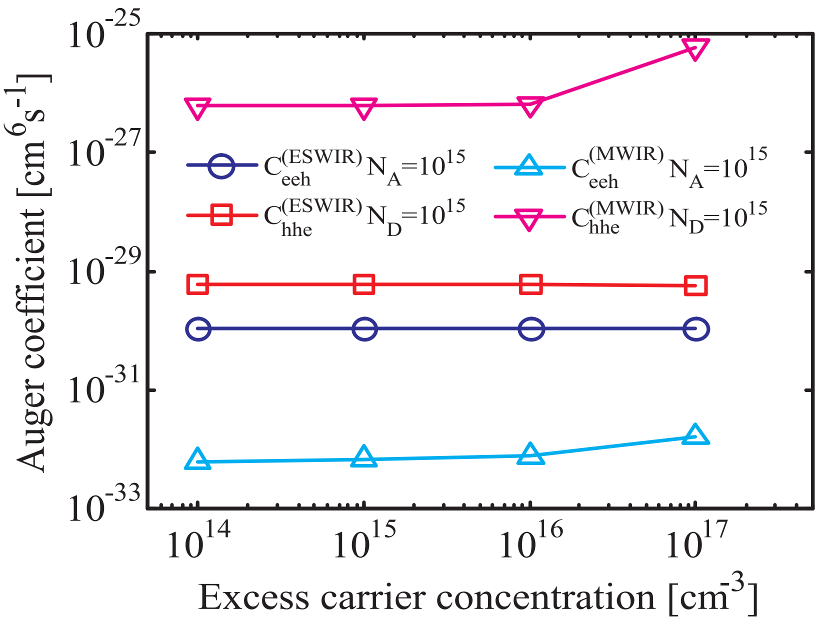

Fig. 16. Auger recombination coefficient function of injection level for doped $Ge_{1-x}Sn_x$ in E-SWIR and MWIR configurations. The doping level is 10^{15} cm^{-3} for both *n*-type and *p*-type.

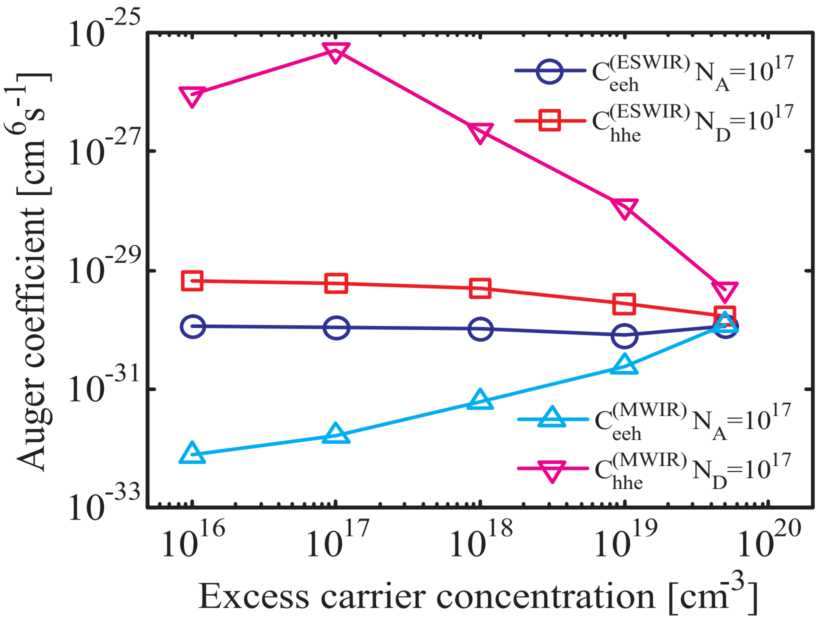

Fig. 17. Auger recombination coefficient function of injection level for doped $Ge_{1-x}Sn_x$ in E-SWIR and MWIR configurations. The doping level is 10^{17} cm^{-3} for both *n*-type and *p*-type.

calculated Auger coefficients for $Ge_{0.82}Sn_{0.18}$ and $Ge_{0.91}Sn_{0.09}$. Therefore, we have performed an additional number of simulations to discern the relative importance of the various contributions. From our analysis, we have concluded that the band structure changes, from $Ge_{0.82}Sn_{0.18}$ to $Ge_{0.91}Sn_{0.09}$, due to different molar fractions is the dominant factor, while differences in the activation energy (i.e. energy gap and phonon energies) play a lesser role. We explain the reduction of Auger coefficient in case of $Ge_{0.82}Sn_{0.18}$ at an injection level higher than 10^{17} cm^{-3} as a saturation in the number of final states available to the secondary particle. The number of these states correlates to the Auger lifetime and the dependence of Auger coefficients on the lifetimes is function of the inverse square of excess carrier concentration (obtained by combining Eqs. (14)-(15) with Eq. (5)). Therefore, the reduction of Auger coefficients in Fig. 17 is the direct consequence of Auger lifetimes saturation in Fig. 10.

4. Conclusions

We have presented a numerical study of the absorption coefficient, radiative and Auger recombination properties of intrinsic and doped $Ge_{1\text{-}x}Sn_x$ at two Sn molar fractions, 9% (E-SWIR) and 18% (MWIR), and temperatures of 240K and 140K, respectively. We have computed the absorption coefficient and radiative recombination rate for the intrinsic material and showed how the emission spectrum changes according to the injection level. Furthermore, we performed a comparison between the radiative and Auger lifetimes given two different doping concentrations for the E-SWIR and MWIR compositions.

As opposed to previous analytical work on Auger recombinations, [42–45] in this work we have applied a Green's function based model to the full electronic band structure of the material, considering the two topmost valence and the two lowest conduction states as possible final states for the scattered particle. Therefore, the relevant contributions that previous analytical works might have neglected, due to applied approximations, have been taken into account in this study.

From this analysis, we concluded that in the E-SWIR case the radiative processes are the dominant recombination mechanism given an injection level lower than 10^{17} cm^{-3} while in the MWIR case the Auger processes are the dominant recombination mechanism above the injection level of 10^{17} cm^{-3}.

Since the present study was aimed at evaluating the potential use of these alloys in detector applications, we have considered only unstrained material. In fact, absorber layers several μm thick may be required for high quantum efficiency photodiodes and these are likely to be relaxed. Nevertheless, for other kinds of applications, such as light emitters, it is likely that strain will play an important role and further investigation is needed.

Funding

Army Research laboratory (ARL) (W911NF-12-2-0023); Army Research Office (ARO) (W911NF-14-1- 0432).

130.192.164.190 {ts '2016-11-08 09:13:04'}